Comparing Differential Reflectivity Arcs Using Phased Array and Conventional Radar Data

ETHAN B. STEWARD*

National Weather Center Research Experiences for Undergraduates Program
Norman, Oklahoma,
Indiana University
Bloomington, Indiana

CHARLES M. KUSTER
NOAA/OAR National Severe Storms Laboratory
Norman, Oklahoma

A. ADDISON ALFORD
NOAA/OAR National Severe Storms Laboratory
Norman, Oklahoma

TERRY J. SCHUUR
NOAA/OAR National Severe Storms Laboratory
Cooperative Institute for Severe and High-Impact Weather Research and Operations
Norman, Oklahoma

VIVEK N. MAHALE
National Weather Service
Norman, Oklahoma

ABSTRACT

Single-polarization phased array radar (PAR), which offers access to rapid-update radar data, has been shown to bring operational benefit to warning decision environments. However, dual-polarization PAR capabilities have remained largely unexplored. In this study, an investigation into the potential operational benefits of dual-polarization PAR data is performed using the Advanced Technology Demonstrator (ATD). The ATD's performance is compared to the National Weather Service radar in Oklahoma City (KTLX). The main dual-polarization signature investigated is the differential reflectivity (Z_{DR}) arc in supercell thunderstorms. Appearance and evolution of Z_{DR} arcs can convey information regarding mesocyclone development and intensification to warning meteorologists. The analysis here focuses on comparing Z_{DR} arcs in ATD and KTLX radar data using both quantitative and qualitative methods. Quantitative analyses will yield explicit differences between the two types of radar, while qualitative analyses help visualize the immediate benefits of dual-polarization PAR data in a warning decision environment. The goal of this study is to explore PAR dual-polarization capabilities in observing the rapidly evolving supercell structures in space and time. It is found that Z_{DR} arcs and their trends are better resolved with the ATD's improved data quality. Additionally, the ATD detected rapidly-evolving signatures, such as Z_{DR} arc disruptions and descending hail cores, faster and clearer than KTLX.

1. Introduction

Since the 1990's, the Weather Surveillance Radar–1988 Dopplers (WSR-88Ds) have been the primary radar used by operational forecasters in the National Weather Service (Crum and Alberty 1993). Since their installation, these radars have been updated and improved as radar

*Corresponding author address: Ethan Steward, Indiana University, 107 S Indiana Ave, Bloomington, IN 47405
E-mail: etbstewa@iu.edu

technology has advanced. For example, by the summer of 2013, all 159 WSR-88D systems were upgraded to dual-polarization capabilities. With the WSR-88D system came operational improvements, such as increased probability of detection of severe weather events and increased warning lead times (Polger et al. 1994; Crum et al. 1998; Doviak et al. 2000). However, the system's lifespan is projected to end around the year 2040 (NWS 2021). Therefore, a large topic of recent meteorological radar research has been focused on replacements that expand upon the existing technology (Hondl and Weber 2019).

One promising candidate for replacement is phased array radar (PAR). Unlike the WSR-88Ds, which leverage a conventional, rotating parabolic antenna, PARs are characterized by a stationary, flat plate antenna from which the radar beam is steered electronically. As a result, PARs can collect volume scans significantly faster than the volume coverage patterns employed by the WSR-88Ds (Weber 2019). In the past twenty years, the National Severe Storms Laboratory (NSSL) found that PARs better depict rapid processes in thunderstorms that a conventional radar could not, such as cell intensification and the evolution of low-level convergence and rotation signatures associated with tornadoes (Forsyth et al. 2005; Heinselman et al. 2008, 2012, 2015). However, little research has been done investigating PAR dual-polarization capabilities, including what potential benefits they may bring.

A variety of dual-polarization signatures have proven to be useful in operational settings, with one being the differential reflectivity (Z_{DR}[1]) arc. Z_{DR} arcs are defined as shallow regions (typically < 2 km in depth) of enhanced Z_{DR} (> 3 dB) commonly located on the rightmost edge of the supercell's forward flank downdraft (FFD) (Kumjian and Ryzhkov 2008; Van Den Broeke 2017). Z_{DR} arcs can be useful to forecasters because they are an indication of hydrometeor size sorting within a storm (Dawson et al. 2014; Van Den Broeke 2020; NWS 2023). Size sorting is the process that results in the varied drop size distribution associated with Z_{DR} arcs (Kumjian and Ryzhkov 2008). Larger raindrops, with larger terminal velocities, fall to the surface quickly after exiting the updraft. However, smaller raindrops, with smaller terminal velocities, will get advected further into the storm's downdraft before reaching the ground. Size sorting is the result of the vertical shear associated with the storm relative wind profile (Dawson et al. 2014). Dawson et al. found that the amount of size sorting in hail and rain fields at a specific level is strongly dependent on the wind profile above that level, throughout the layer that precipitation is falling. Therefore, the presence of a Z_{DR} arc suggests that the storm's inflow air has a veering vertical profile. As a result, Z_{DR} arcs are signs that a storm's low-level mesocyclone may intensify, especially when it extends towards the storm's inflow notch (Kumjian 2013b). Analogously, storms exhibiting a Z_{DR} arc without a rotating updraft may develop a mesocyclone and become more supercellular in nature.

Another potentially useful aspect of Z_{DR} arcs is that their characteristics may also provide information about the thermodynamic characteristics of air currents that can enter the updraft. Markowski and Richardson (2014) found that the likelihood for tornadogenesis in supercells is greatest when cold pools are of intermediate strength (i.e., not too cold). A disruption of the Z_{DR} arc can reveal the presence of a relatively cold downdraft within the forward flank of the supercell near the hook echo (NWS 2023). Z_{DR} arc disruptions containing wet, melting hail imply that the intruding air is negatively buoyant, thus strengthening the storm's cold pool and potentially inhibiting tornadogenesis. On the other hand, no definite conclusion can be made regarding tornadogenesis potential with dry hail Z_{DR} arc disruptions, as their thermodynamic properties are not obvious and can vary (NWS 2023).

Since Z_{DR} arcs likely have implications for supercell evolution and potential hazards, the purpose of this study is to compare the structure and evolution of Z_{DR} arcs with PAR and WSR-88D data to examine potential advantages of dual-polarization PAR. This comparison is performed both qualitatively and quantitatively to find explicit differences in Z_{DR} arc depictions while also exploring whether these differences would bring operational benefit in a warning decision environment.

2. Data and Methods

In 2018, the NSSL received the Advanced Technology Demonstrator (ATD). The ATD is the first S-band, dual-polarization PAR purposely built for meteorological purposes (Torres and Wasielewski 2022). It rests on a 10-meter tower enclosed by a spherical radome. The radar can observe a 90° sector at any given time and sits on an azimuthal turntable that allows 360° motion, enabling radar operators to sample storms in any direction. The radar has 4,864 radiating elements that enable electronic steering of the radar beam. It is operated manually through a Human-Machine-Interface (HMI), allowing the operators to create specific scanning strategies and visualize live radar data (Torres and Curtis 2022).

The comparison between the ATD and nearest operational WSR-88D (KTLX) will be conducted through two cases: 23 April 2022 (2326 UTC - 0016 UTC) and 11 May 2023 (2330 UTC - 0119 UTC). Both cases feature tornadic supercells within 50 km of the radars. Non-tornadic supercell cases are not considered due to a lack of recorded cases in close proximity to the ATD. The two radars are about 20 kilometers apart, with the ATD due

[1] Z_{DR} is a measure of the difference of returned power between the horizontal and vertical channels (Kumjian 2013a). Hydrometeors with a more oblate orientation (i.e., large raindrops) will have larger Z_{DR} values, while spherical objects (e.g., small hail) will have Z_{DR} values near zero.

TABLE 1. Details of the ATD and KTLX elevation angles employed on 23 April 2022 and 11 May 2023.

VCP Name	Radar	Elevation Angles (°)
VCP212	KTLX	0.5, 0.9, 1.3, 1.8, 2.4, 3.1, 4.0, 5.1, 6.4, 8.0, 10.0, 12.5, 15.6, 19.5
VCP212	ATD (23 April)	0.5, 0.9, 1.3, 0.5, 1.8, 2.4, 3.1, 4.0, 0.5, 5.1, 6.4, 8.0, 0.5, 10.0, 12.5, 15.6, 19.5
SUPERCELL	ATD (11 May)	0.5, 0.9, 1.3, 1.8, 2.4, 3.1, 4.0, 5.1, 0.5, 5.8, 6.4, 7.2, 8.0, 9.0, 10.0, 11.0, 12.5, 15.6, 19.5, 23.4

southwest of KTLX. Case start and end times were determined by ATD data availability. Storm reports for 23 April were provided by the National Center for Environmental Information's Storm Events Database (available at `https://www.ncdc.noaa.gov/stormevents/`). The reports for 11 May were provided by the National Weather Service's Damage Assessment Toolkit (available at `https://apps.dat.noaa.gov/stormdamage/damageviewer/`).

In both cases, the ATD leveraged special scanning strategies using similar methods to the Supplemental Adaptive Intravolume Low-Level Scans (SAILS; NWS 2012). Specifically, the ATD employed intra-volume revisits to the 0.5° elevation, similar to the SAILS technique employed by the WSR-88Ds. The ATD scanned in 90° sectors, while KTLX traditionally scanned 360°. KTLX was operated with Volume Coverage Pattern (VCP) 212 for both cases, often with SAILS cuts employed. The ATD was operated with elevation angles that mimicked VCP 212 on 23 April and with a custom VCP developed by the radar operators on 11 May. This custom VCP has several extra elevation angles in addition to the traditional VCP 212 elevation angles to sample storms with increased vertical resolution. On 23 April, the ATD operated with akin to SAILS 3 (meaning that four 0.5° elevation cuts were collected per radar volume) beginning at 2347 UTC, while KTLX operated with SAILS 2 (three 0.5° elevations per radar volume). Full volume scans were generated approximately every 90 seconds with the ATD and every six minutes with KTLX. The lowest elevation (0.5°) scans for the ATD are produced every twenty seconds on average and every two minutes for KTLX. Similarly, on 11 May, the ATD operated akin to SAILS 1 (two 0.5° cuts per radar volume) and KTLX also with SAILS 1. The ATD produced full volume scans approximately every 100 seconds and, again, KTLX every six minutes. Lowest elevation scans were produced by the ATD every minute and every two minutes by KTLX. Additional information regarding the ATD and KTLX scanning strategies for these cases is displayed in Table 1.

Analysis in this study consists of qualitative and quantitative portions. For qualitative analysis, data from each radar were subjectively compared, and timelines were constructed for both radars that contained information about Z_{DR} arc appearances and trends in the low-level scans. The timelines were then compiled together to discern the largest differences between the ATD and KTLX. Differences in beam height between the two radars were minimized when comparing Z_{DR} arcs by selecting appropriate elevation angles from each radar. The goal with the qualitative analysis was to determine how the two types of radar compare operationally to discern potential benefits a PAR could bring to a warning decision environment. For the quantitative analysis, Z_{DR} arc area, mean value, median value, and standard deviation were captured throughout the storms' lifetimes with both datasets using the Supercell Polarimetric Observation Research Kit (SPORK; Wilson and Van Den Broeke 2022). Time series of these variables were then created to directly compare the two radars, highlighting key differences in their Z_{DR} arc characteristics. The goal with this analysis was to quantify the improvement PARs bring with data quality and resolution, both spatially and temporally.

3. Results

a. 23 April 2022 Supercell

On this day, a cluster of thunderstorms and supercells developed ahead of a stalling dryline. Central and southwest Oklahoma saw damaging winds, hail, and a few weak tornadoes. The main supercell of interest was already present when the ATD began collecting data at 2326 UTC. The storm was located in northeastern Caddo County and northwestern Grady County and was moving northeast at approximately 55 kilometers per hour. The supercell also already exhibited dual-polarization signatures consistent with hail and Z_{DR} arcs observed by both radars at this time.

At 2336 UTC, the ATD depicted a hail core at approximately 3.2 km above radar level (ARL) (Fig. 1a). Approximately a minute later, the ATD displayed the same core at 2.4 km (Fig. 1b). The hail core is then seen in KTLX at 1.9 km ARL at 2338 UTC (Fig. 1c). Shortly after, the hail core is present at 1.4 km in the ATD (Fig. 1d). A minute later, at 2339 UTC, the ATD's lowest elevation scan depicts the hail core at 0.6 km (Fig. 1e). The next available KTLX scan at a height lower than 1.9 km ARL

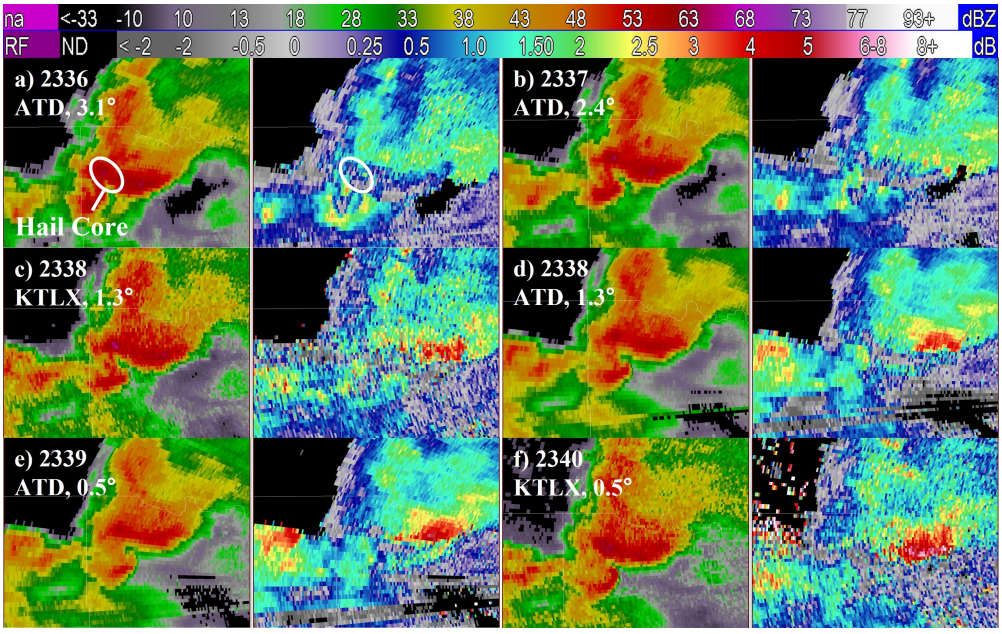

FIG. 1. The descent of the 23 April supercell's hail core with the ATD and KTLX. Scans are in chronological order. (a) First scan showing hail core at 3.1°, with reflectivity (Z) on the left and Z_{DR} on the right. (b)-(f) As in (a), but for different radar tilts.

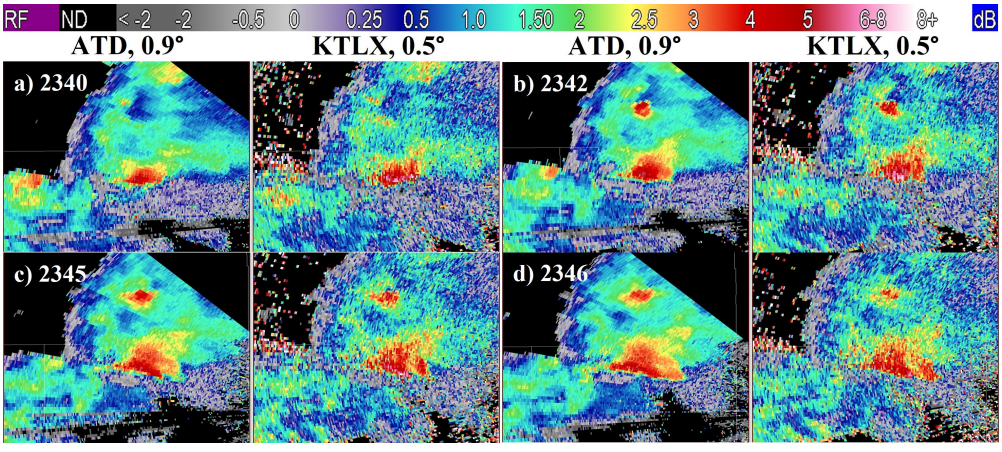

FIG. 2. The evolution of the Z_{DR} arc disruption with both radars. (a) ATD imagery is on the left in each subplot and KTLX is on the right for 2340 UTC. (b)-(d) As in (a), but for different times.

(Fig. 1c), occurs at 2340 UTC, and shows the hail core at 0.9 km ARL (Fig. 1f). In contrast to KTLX, the rapid-update volume scans provided by the ATD captured the descent of the hail core without any large spatial or temporal gaps. Additionally, the hail core was present at the ATD's lowest elevation scan a minute faster than that of KTLX. Also, the Z_{DR} ATD data were visually less noisy than that of KTLX. With improved Z_{DR} data quality and temporal resolution over KTLX, the ATD data better capture the hail core's structure and temporal descent, under which a two inch hail report was later made at 2347 UTC.

As the hail core descended and began enlarging at the low-levels, both radars depict a Z_{DR} arc disruption around at 2340 UTC (Fig. 2a). At 2342 UTC, ATD data show the Z_{DR} arc redeveloping and the Z_{DR} arc disruption shrinking, while the KTLX scan 25 seconds later still shows a fully disrupted Z_{DR} arc (Fig. 2b). Three minutes later, the ATD depicts the Z_{DR} arc to be fully redeveloped. However, KTLX still features Z_{DR} $\sim$0 dB in this area, indicating that the arc is still disrupted (Fig. 2c). By 2346 UTC, both radars display redeveloped Z_{DR} arcs (Fig. 2d). The difference in Z_{DR} arc disruption timing is noteworthy because even though both radars display a Z_{DR} arc disruption, the

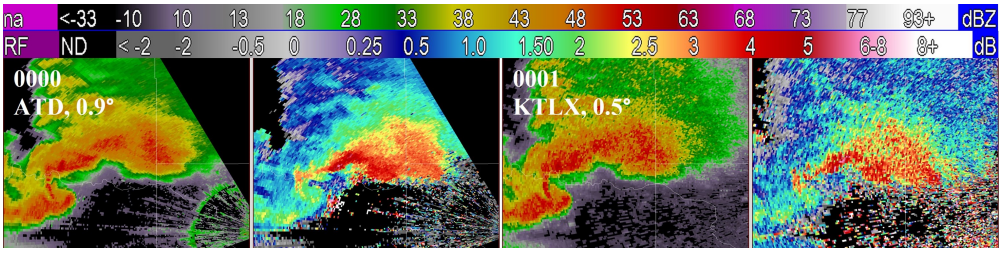

FIG. 3. The line of high Z_{DR} wrapping into the 23 April supercell's hook echo around 0000 UTC. The left panel of each subplot displays ATD imagery and the right displays KTLX.

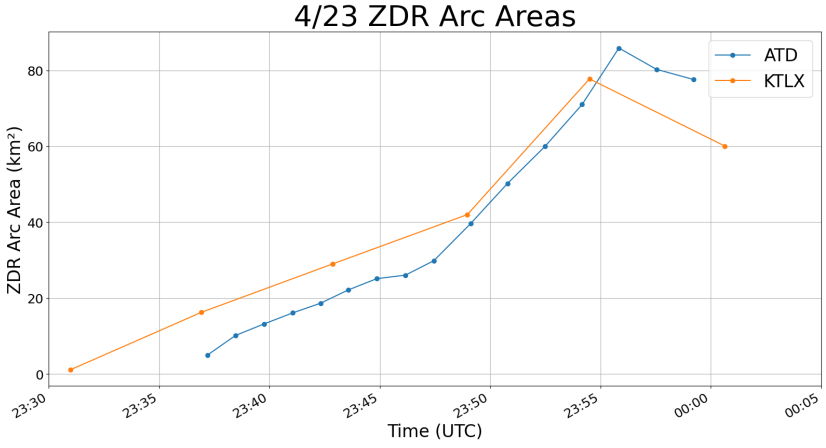

FIG. 4. A time series of the 23 April supercell's Z_{DR} arc areas generated from SPORK output. The blue line represents the ATD Z_{DR} arc and the orange represents KTLX.

longer-lasting disruption depicted by KTLX is more suggestive of decreased tornadogenesis potential for a longer period of time than actually occurred.

After the disruption, the supercell Z_{DR} arc undergoes a period of constant growth with both radars, spanning the entire forward flank reflectivity gradient (FFRG). At 0001 UTC, an EF-0 tornado begins in northern Grady County. At this time, both radars display a hook echo in reflectivity. However, the ATD displays a discernable line of high Z_{DR} wrapped into the hook echo, while KTLX does not (Fig 3). The Z_{DR} arc with the ATD is also much smoother than that of KTLX. The tornado lasts until 0010 UTC, with both radars showing high Z_{DR} (> 2 dB) wrapping into the hook echo. Shortly after, the supercell moves out of the ATD's scanning sector, marking the end of the case for this study.

Utilizing data output from SPORK, a time series of this supercell's Z_{DR} arc area for both radars is generated (Fig. 4). Each data point in Fig. 4 corresponds to a radar volume scan interpreted by SPORK, so the increased temporal data resolution that the ATD offers over KTLX is apparent, given the larger amount of data points. Both radars show the same general trends with their Z_{DR} arcs over time. The arcs continually grow in size until about 2355 UTC, after which they begin getting smaller. The increased temporal resolution of the ATD does resolve the arc's evolution in greater detail, but the magnitude and trends in Z_{DR} arc area are quite similar between the two radars. In this case, with a large, well-defined Z_{DR} arc, differences in temporal resolution and data quality may not greatly impact SPORK's ability to quantify Z_{DR} arc area. However, as discussed above, differences in temporal resolution and data quality certainly matter when assessing the Z_{DR} arc qualitatively.

b. 11 May 2023 Supercells

On this day, thunderstorms formed in southwestern Oklahoma ahead of a dryline and moved into central Oklahoma. Similar to the previous case, these storms went on to produce severe hail and tornadoes. At 2330 UTC, two distinct storms are present southwest of both the ATD and KTLX in Grady County. The northern storm (Figs. 5–7) and southern storm (Figs. 8 and 9) both become supercells with accompanying Z_{DR} arcs sampled by the ATD.

At 2337 UTC, the northern storm starts inheriting supercellular characteristics and also begins elongating, resulting in a long, narrow FFD and Z_{DR} arc. The arc spans

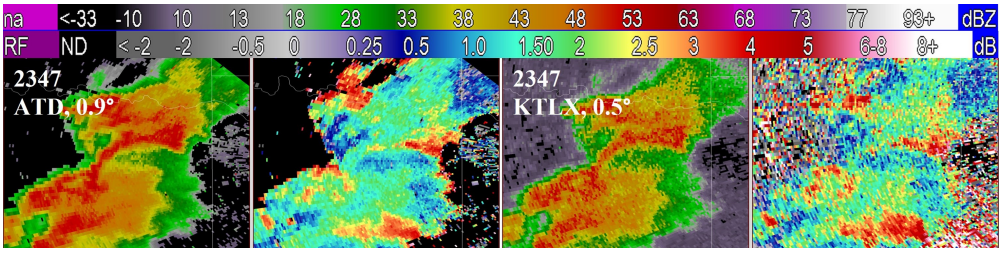

FIG. 5. The differing depictions of the 11 May northern supercell's Z_{DR} arc at 2347 UTC. The two left panels display ATD imagery and the two right panels display KTLX.

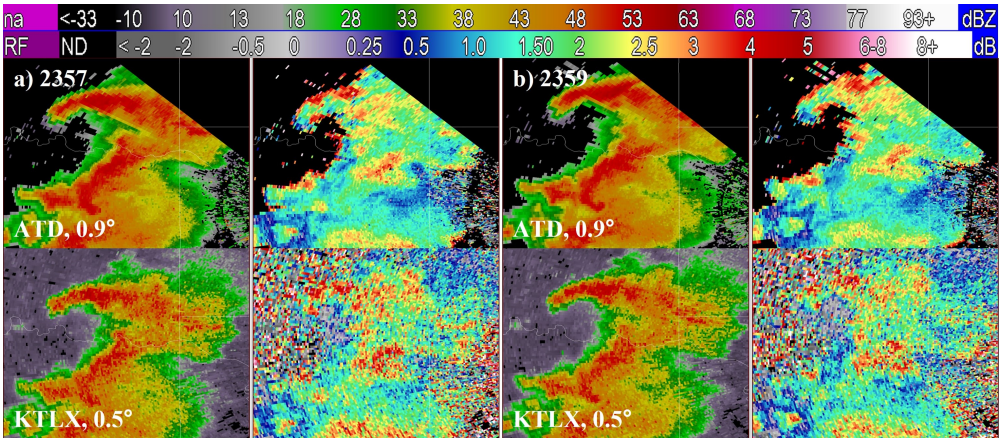

FIG. 6. As in Fig. 5, but with the top panel displaying ATD imagery and the bottom displaying KTLX at (a) 2357 UTC and (b) 2359 UTC.

the entire FFRG in both the ATD and KTLX data. Starting around 2345 UTC, both arcs begin taking on lower values, continuing for the next few scans. The forward flank region near the updraft specifically features Z_{DR} values around 1.5–2 dB. At 2347 UTC, the ATD still observes a continuous stream of Z_{DR} ∼2 dB, while KTLX does not (Fig. 5). The more visible arc in the ATD data allows for easier recognition that the arc is still present and size sorting is still occurring. However, this difference is quickly minimized in the next few ATD and KTLX scans, at which the Z_{DR} arc once again contains higher values. At 2357 UTC, the supercell produces an EF-U tornado. Three minutes later, KTLX depicts a visually noisier and larger core of high Z_{DR} within the arc than the ATD (Fig. 6a). Here the shape of the remaining Z_{DR} arc is difficult to discern with KTLX, but is clearer in ATD data. The next KTLX scan still shows a larger Z_{DR} core than that observed by the ATD (Fig. 6b). Additionally, a line of enhanced Z_{DR} can be seen wrapping into the supercell's hook echo in the ATD. At 0003 UTC, both radars show that the Z_{DR} arc is weakening by taking on lower values (Fig. 7a). However, the remaining portions of the arc are more visible in the ATD imagery, as the arc in KTLX is visually noisy. The same can be seen a minute later, with the diminishing arc becoming increasingly noisy in KTLX (Figs. 7b and 7c). The scans at 0008 UTC showcase the arc's end, with most Z_{DR} values in the area below 2.5 dB with the ATD and variable Z_{DR} in KTLX (Fig. 7d). From Fig. 7, the increased Z_{DR} data quality of the ATD makes it easier to see when the Z_{DR} arc ends. The tornado was estimated to have ended also at 0008 UTC.

Similarly to the northern storm, the southern storm exhibits supercellular characteristics by 2338 UTC. At 0038 UTC, an EF-0 tornado develops and lasts for less than a minute. By this time, the supercell has both an elongated shape and Z_{DR} arc. Both radars depict the Z_{DR} arc along the supercell's entire FFRG, with high Z_{DR} values wrapped around inside the hook echo (Fig. 8a). The arc in the ATD, however, is smoother and better displays the supercell's Z_{DR} gradient, giving greater indication that the storm is undergoing size sorting. The same can be seen at 0040 UTC, where the Z_{DR} arc's shape is difficult to discern in KTLX (Fig. 8b). Two minutes later, the supercell produces another EF-0 tornado. Around 0044 UTC, the ATD displays a Z_{DR} arc with a discernable line of enhanced Z_{DR} wrapping into the storm's hook echo (Fig. 9a). KTLX also displays the Z_{DR} arc, but not the hook echo wrapping. Approximately two minutes later, the same hook echo wrapping is still apparent in the ATD, but not KTLX (Fig. 9b). Additionally, the Z_{DR} arc in KTLX is not as well defined

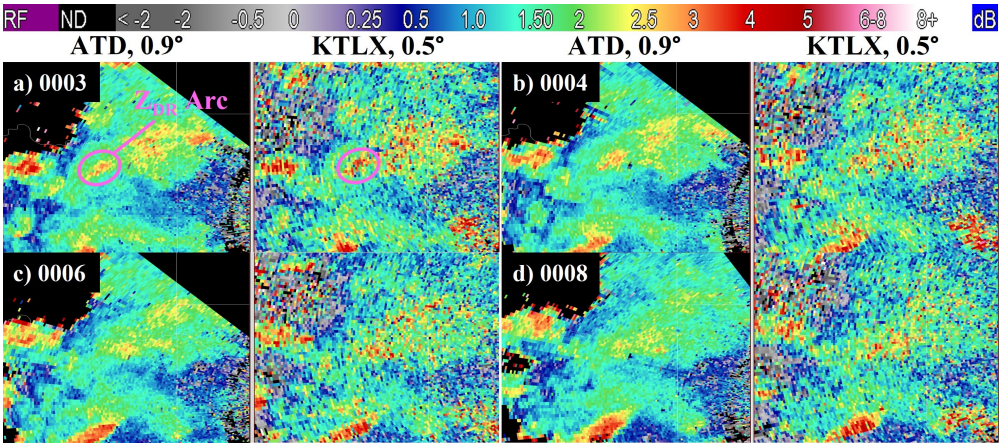

FIG. 7. The end of the 11 May northern supercell's Z_{DR} arc. (a) The left panel displays ATD imagery and the right displays KTLX at 0003 UTC. (b)-(d) As in (a), but for different times.

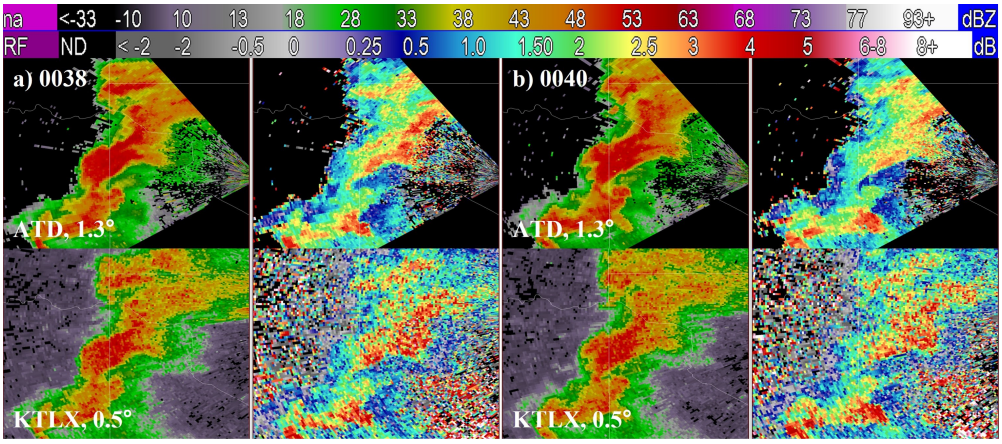

FIG. 8. The differing depictions of the 11 May southern supercell's Z_{DR} arc and Z_{DR} gradient. The top two panels in each subplot display ATD imagery and the bottom two display KTLX at 0038 UTC (a) and 0040 UTC (b).

in this scan as its ATD counterpart. The storm's tornado ends at 0049 UTC. Two minutes after, the storm appears to be losing its supercellular structure, with the Z_{DR} arc remains becoming smaller in the ATD and indiscernible with KTLX (Fig. 9c). Both radars show the arc gone by 0054 UTC (Fig. 9d).

Similar to Fig. 4, a time series for the northern supercell's Z_{DR} arc's areas for both radars in this case is created with SPORK output (Fig. 10). Unlike the Z_{DR} arc from 23 April 2022, the arcs in this case were often elongated and consisted of lower Z_{DR} values (less than 3 dB). Consequently, with both the ATD and KTLX, SPORK was unable to fully resolve the Z_{DR} arcs for many volume scans. This is apparent in Fig. 10, where the areas of the ATD's Z_{DR} arc are displayed to have spontaneous, irregular periods of growth and decay. However, large differences between the two radars exist here. The areas representing the arc in KTLX are unrepresentative of those depicted in radar imagery, with the maximum size being below five square km. On the contrary, SPORK registers a larger Z_{DR} arc with the ATD data, more accurately representing the arc's true sizes. Additionally, around 2350 UTC, there does not exist a data point representing the Z_{DR} arc in KTLX. However, SPORK is still outputting data for the ATD's arc at this time. This suggests a potential increase in SPORK's ability to detect Z_{DR} arcs when using the ATD's polarimetric data. SPORK struggled to properly sample the second Z_{DR} arc with both radars, once again showing abrupt trends in arc areas and full volume scans without an accompanying arc (not shown). With that said, SPORK still managed to recognize a Z_{DR} arc more often in ATD data.

4. Conclusions

This study investigated PAR dual-polarization capabilities by comparing Z_{DR} arcs in supercells depicted by the

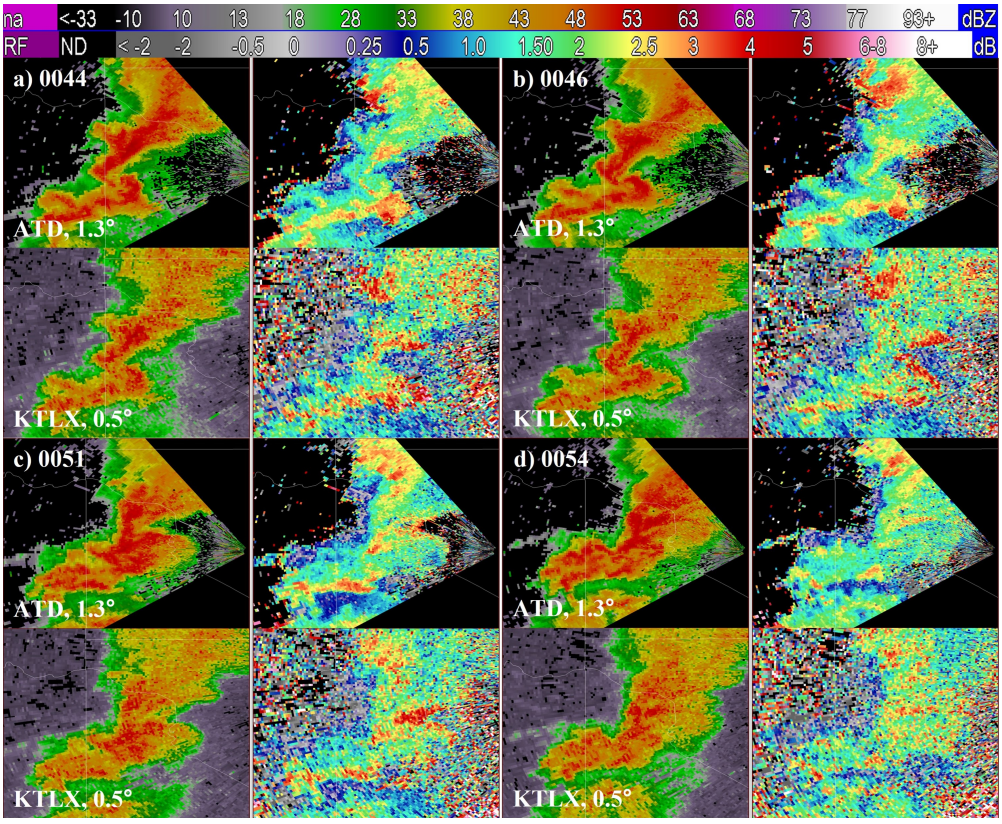

FIG. 9. The differing depictions of the 11 May southern supercell's Z_{DR} arc. The top panels in each subplot displays ATD imagery and the bottom panels display KTLX. The line of high Z_{DR} can be seen wrapping into the 11 May southern supercell's hook echo at 0044 UTC (a) and 0046 UTC (b). The end of the 11 May southern supercell's Z_{DR} arc is depicted in (c) and (d).

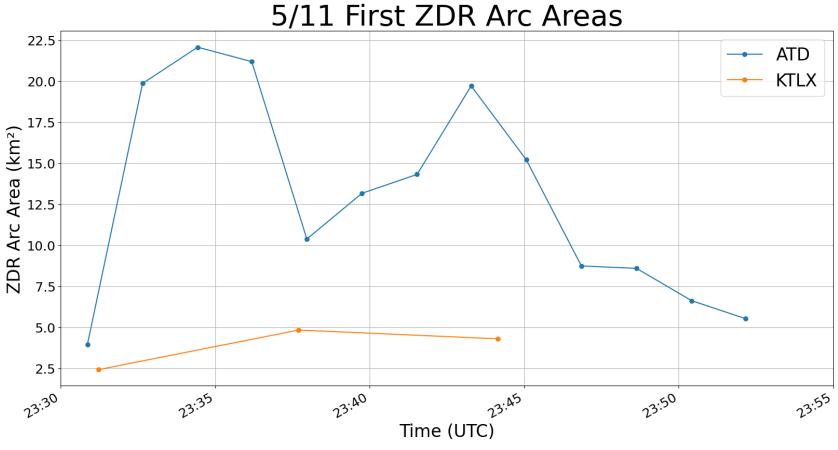

FIG. 10. As in Fig. 4, but for the 11 May northern supercell's Z_{DR} arc areas.

ATD and KTLX. Two cases were chosen for comparison, 23 April 2022 and 11 May 2023. Both days contained tornadic supercells with accompanying Z_{DR} arcs within 50 kilometers of both radars. Analysis was conducted both qualitatively and quantitatively to allow for explicit comparison in radar performance while exploring whether their differences would be operationally relevant. The main findings of this study are the following:

- The ATD features better data quality than KTLX regarding Z_{DR} and other dual-polarization products. Z_{DR} arcs were generally easier to detect and smoother in ATD data than with KTLX. Small scale features, such as the wrapping of enhanced Z_{DR} into the hook echo during ongoing tornadoes, were both easier to discern and more detailed with the ATD (Figs. 3 and 9). Z_{DR} gradients across supercells were also easier to identify, providing greater confidence of ongoing size sorting (Fig. 8).

- Greater temporal resolution with the ATD allowed for both faster updates and detection of dual-polarization signatures than with KTLX. The ATD was able to track the descent of a severe hail core from the mid-levels, while KTLX only captured the core once aloft and then once again when it had already arrived at the lowest elevation scan (Fig. 1). Additionally, the ATD captured smoother trends with Z_{DR} arc disruptions, showcasing their gradual beginnings and endings, rather than rapid changes depicted by KTLX (Fig. 2).

- The quantitative analyses conducted by SPORK, particularly with the 11 May 2023 case, suggest that the ATD data quality may increase algorithms' capabilities in automatically detecting Z_{DR} arcs. The Z_{DR} arc areas measured by SPORK are more representative with the ATD data than with KTLX (Fig. 10). Additionally, there exists a KTLX volume scan where SPORK did not recognize a Z_{DR} arc while areas were still being measured with the ATD.

This study served as one of the first investigations into dual-polarization PAR data quality and its comparison to WSR-88D data. It was found that the ATD data quality was improved over KTLX, which allowed for more defined gradients in Z_{DR} and better detection of small-scale features. Such improvements are most likely primarily attributed to the advanced signal processing techniques being actively developed and tested on the ATD akin to range oversampling developed by Curtis and Torres (2014) in addition to PAR-related advantages such as the lack of beam smearing. The increased resolution of rapidly evolving dual-polarization signatures with the ATD are consistent with the findings of by Heinselman et al. (2008, 2012, 2015), who noted the operational benefit from increased temporal resolution with single-polarization PAR. Although the denser vertical sampling afforded by the ATD was not directly examined here due to the low-level nature of Z_{DR} arcs, it is expected that the ATD's denser vertical sampling capabilities will lead to further increased resolution of the evolution of polarimetric supercell signatures. Indeed the tracking of a descending hail core in space and time that disrupted a Z_{DR} arc (Figs. 1 and 2) was substantially improved leveraging ATD data.

Future research is required to further investigate PAR dual-polarization capabilities, especially regarding correlation coefficient (CC) and specific differential phase (K_{DP}). This study was unable to investigate non-tornadic supercell cases, which should be a focus when studying Z_{DR} arcs and especially Z_{DR} arc disruptions. Also, other common supercell polarimetric signatures were not analyzed here, such as the Z_{DR} and K_{DP} column, K_{DP} foot, and tornadic debris signature (TDS). However, it is concluded that, with their increased spatiotemporal resolution, dual-polarization PARs provide forecasters with quicker, more precise updates on rapidly evolving polarimetric signatures, particularly regarding Z_{DR} arcs.

Acknowledgments. I would like to thank the National Science Foundation for the opportunity to perform research this summer at the National Weather Center and University of Oklahoma, whom I also thank for graciously hosting the REU program. Next, I want to thank Alex Marmo and Daphne LaDue for directing the program, providing us with a myriad of amazing experiences, and supporting us throughout the entire journey. Finally, I would like to give a huge thank you to my fellow co-authors and mentors for everything they have done for me. Charles, Addison, Terry, and Vivek–thank you so much for all of the guidance, support, continuous teaching, and memories this summer. Funding was provided by the NSF grant AGS. 2050267.

References

Crum, T. D., and R. L. Alberty, 1993: The WSR-88D and the WSR-88D Operational Support Facility. *Bulletin of the American Meteorological Society*, **74 (9)**, 1669–1688, doi:10.1175/1520-0477(1993)074<1669:TWATWO>2.0.CO;2, URL https://doi.org/10.1175/1520-0477(1993)074<1669:TWATWO>2.0.CO;2.

Crum, T. D., R. E. Saffle, and J. W. Wilson, 1998: An Update on the NEXRAD Program and Future WSR-88D Support to Operations. *Weather and Forecasting*, **13 (2)**, 253–262, doi:10.1175/1520-0434(1998)013<0253:AUOTNP>2.0.CO;2, URL http://journals.ametsoc.org/doi/10.1175/1520-0434(1998)013<0253:AUOTNP>2.0.CO;2.

Curtis, C. D., and S. M. Torres, 2014: Adaptive Range Oversampling to Improve Estimates of Polarimetric Variables on Weather Radars. *Journal of Atmospheric and Oceanic Technology*, **31 (9)**, 1853–1866, doi:10.1175/JTECH-D-13-00216.1, URL http://journals.ametsoc.org/doi/10.1175/JTECH-D-13-00216.1.

Dawson, D. T., E. R. Mansell, Y. Jung, L. J. Wicker, M. R. Kumjian, and M. Xue, 2014: Low-Level ZDR Signatures in Supercell Forward Flanks: The Role of Size Sorting and Melting of Hail. *Journal of the Atmospheric Sciences*, **71 (1)**, 276–299, doi:10.1175/JAS-D-13-0118.1, URL https://journals.ametsoc.org/doi/10.1175/JAS-D-13-0118.1.

Doviak, R. J., V. Bringi, A. Ryzhkov, A. Zahrai, and D. Zrnić, 2000: Considerations for Polarimetric Upgrades to Operational WSR-88D Radars. *Journal of Atmospheric and Oceanic Technology*, **17 (3)**, 257–278, doi:10.1175/1520-0426(2000)017<0257:

CFPUTO>2.0.CO;2, URL http://journals.ametsoc.org/doi/10.1175/1520-0426(2000)017<0257:CFPUTO>2.0.CO;2.

Forsyth, D. E., and Coauthors, 2005: The National Weather Radar Testbed (Phased-Array). *32nd Conference on Radar Meteorology*, Albuquerque, New Mexico, URL https://ams.confex.com/ams/pdfpapers/96377.pdf.

Heinselman, P., D. LaDue, D. M. Kingfield, and R. Hoffman, 2015: Tornado Warning Decisions Using Phased-Array Radar Data. *Weather and Forecasting*, **30 (1)**, 57–78, doi:10.1175/WAF-D-14-00042.1, URL https://journals.ametsoc.org/doi/10.1175/WAF-D-14-00042.1.

Heinselman, P. L., D. S. LaDue, and H. Lazrus, 2012: Exploring Impacts of Rapid-Scan Radar Data on NWS Warning Decisions. *Weather and Forecasting*, **27 (4)**, 1031–1044, doi:10.1175/WAF-D-11-00145.1, URL https://journals.ametsoc.org/doi/10.1175/WAF-D-11-00145.1.

Heinselman, P. L., D. L. Priegnitz, K. L. Manross, T. M. Smith, and R. W. Adams, 2008: Rapid Sampling of Severe Storms by the National Weather Radar Testbed Phased Array Radar. *Weather and Forecasting*, **23 (5)**, 808–824, doi:10.1175/2008WAF2007071.1, URL https://journals.ametsoc.org/doi/10.1175/2008WAF2007071.1.

Hondl, K., and M. Weber, 2019: NOAA's Meteorological Phased Array Radar Research Program. *2019 IEEE International Symposium on Phased Array System & Technology (PAST)*, IEEE, Waltham, MA, USA, 1–6, doi:10.1109/PAST43306.2019.9020994, URL https://ieeexplore.ieee.org/document/9020994/.

Kumjian, M., 2013a: Principles and applications of dual-polarization weather radar. Part I: Description of the polarimetric radar variables. *Journal of Operational Meteorology*, **1 (19)**, 226–242, doi:10.15191/nwajom.2013.0119, URL http://nwafiles.nwas.org/jom/articles/2013/2013-JOM19/2013-JOM19.pdf.

Kumjian, M., 2013b: Principles and applications of dual-polarization weather radar. Part II: Warm- and cold-season applications. *Journal of Operational Meteorology*, **1 (20)**, 243–264, doi:10.15191/nwajom.2013.0120, URL http://nwafiles.nwas.org/jom/articles/2013/2013-JOM20/2013-JOM20.pdf.

Kumjian, M. R., and A. V. Ryzhkov, 2008: Polarimetric Signatures in Supercell Thunderstorms. *Journal of Applied Meteorology and Climatology*, **47 (7)**, 1940–1961, doi:10.1175/2007JAMC1874.1, URL http://journals.ametsoc.org/doi/10.1175/2007JAMC1874.1.

Markowski, P. M., and Y. P. Richardson, 2014: The Influence of Environmental Low-Level Shear and Cold Pools on Tornadogenesis: Insights from Idealized Simulations. *Journal of the Atmospheric Sciences*, **71 (1)**, 243–275, doi:10.1175/JAS-D-13-0159.1, URL https://journals.ametsoc.org/doi/10.1175/JAS-D-13-0159.1.

NWS, 2012: Supplemental Adaptive Intra-Volume Low-Level Scan (SAILS). Tech. rep., NOAA. URL https://www.roc.noaa.gov/WSR88D/PublicDocs/NewTechnology/Supplemental_Adaptive_Intra_Volume_Low_Level_Scan_Description_Document_Final.pdf.

NWS, 2021: NEXRAD Strategic Plan 2021 – 2025. Tech. rep., NOAA. URL https://www.roc.noaa.gov/WSR88D/PublicDocs/NEXRAD_Strategic_Plan_2021-2025_May%202021_v5.pdf.

NWS, 2023: Training Resources. Tech. rep., NOAA. URL https://sites.google.com/a/noaa.gov/nws-cr-tornado-warning-improvement-project/training-resources.

Polger, P. D., B. S. Goldsmith, R. C. Przywarty, and J. R. Bocchieri, 1994: National Weather Service Warning Performance Based on the WSR-88D. *Bulletin of the American Meteorological Society*, **75 (2)**, 203–214, doi:10.1175/1520-0477(1994)075<0203:NWSWPB>2.0.CO;2, URL http://journals.ametsoc.org/doi/10.1175/1520-0477(1994)075<0203:NWSWPB>2.0.CO;2.

Torres, S., and C. Curtis, 2022: Untapped Capabilities of the Advanced Technology Demonstrator at the National Severe Storms Laboratory. *2022 IEEE International Symposium on Phased Array Systems & Technology (PAST)*, IEEE, Waltham, MA, USA, 1–5, doi:10.1109/PAST49659.2022.9975029, URL https://ieeexplore.ieee.org/document/9975029/.

Torres, S., and D. Wasielewski, 2022: The Advanced Technology Demonstrator at the National Severe Storms Laboratory: Challenges and Successes. *2022 IEEE Radar Conference (RadarConf22)*, IEEE, New York City, NY, USA, 1–6, doi:10.1109/RadarConf2248738.2022.9764231, URL https://ieeexplore.ieee.org/document/9764231/.

Van Den Broeke, M. S., 2017: Polarimetric Radar Metrics Related to Tornado Life Cycles and Intensity in Supercell Storms. *Monthly Weather Review*, **145 (9)**, 3671–3686, doi:10.1175/MWR-D-16-0453.1, URL https://journals.ametsoc.org/doi/10.1175/MWR-D-16-0453.1.

Van Den Broeke, M. S., 2020: A Preliminary Polarimetric Radar Comparison of Pretornadic and Nontornadic Supercell Storms. *Monthly Weather Review*, **148 (4)**, 1567–1584, doi:10.1175/MWR-D-19-0296.1, URL http://journals.ametsoc.org/doi/10.1175/MWR-D-19-0296.1.

Weber, M. E., 2019: Meteorological Phased Array Radar Research at NOAA's National Severe Storms Laboratory. *2019 IEEE International Conference on Microwaves, Antennas, Communications and Electronic Systems (COMCAS)*, IEEE, Tel-Aviv, Israel, 1–6, doi:10.1109/COMCAS44984.2019.8958067, URL https://ieeexplore.ieee.org/document/8958067/.

Wilson, M. B., and M. S. Van Den Broeke, 2022: Using the Supercell Polarimetric Observation Research Kit (SPORK) to Examine a Large Sample of Pretornadic and Nontornadic Supercells. *E-Journal of Severe Storms Meteorology*, **17 (2)**, 1–38, doi:10.55599/ejssm.v17i2.85, URL https://ejssm.com/ojs/index.php/site/article/view/85.